Research Square

Preprints are preliminary reports that have not undergone peer review.
They should not be considered conclusive, used to inform clinical practice,
or referenced by the media as validated information.

Research on Thermal Error Prediction Technology of Ultra-Precision Machine Tool Spindle

yuqing tang

tangyuqing@iet.cn

Institute of Engineering Thermophysics Chinese Academy of Sciences

Hao ZHONG
Jun YAO
Shuai SU
Baorui DU
Jun TANG
Guangzhe ZHOU

Research Article

Keywords: Ultra-precision Motorized Spindle, Thermal Error Prediction, Thermal Resistance Network, LSTM-PDE

Posted Date: March 2nd, 2026

DOI: https://doi.org/10.21203/rs.3.rs-8877388/v1

License: This work is licensed under a Creative Commons Attribution 4.0 International License.
Read Full License

Version of Record: A version of this preprint was published at The International Journal of Advanced Manufacturing Technology on July 28th, 2026. See the published version at https://doi.org/10.1007/s00170-026-18813-z.

Research on Thermal Error Prediction Technology of Ultra-Precision Machine Tool Spindle

TANG Yuqing[①②],ZHONG Hao[①],YAO Jun[①],SU Shuai[①],DU Baorui[①],TANG Jun[④],ZHOU Guangzhe[④]

(①The Institute of Engineering Thermophysics, Chinese Academy of Sciences, Beijing，100190，CHN;②Research Center of Fluid Machinery Engineering and Technology,Jiangsu University, Jiangsu,212013，CHN;③Huacui Intelligent Assembly Co., Ltd.，Jiangsu，225500，CHN;④Shanghai Aircraft Manufacturing Co., Ltd., Commercial Aircraft Corporation of China, Shanghai, 201324, CHN)

First Author: Tang Yuqing (2002－), Female, Graduate Student. Research area: Thermal management of CNC machine tools.

E-mail: tangyuqing@iet.cn

Corresponding Author: Yao Jun (1988－), Male, Ph.D., Senior Engineer. Research area: Thermal control of load-bearing structures, thermal management of CNC machine tools.

E-mail: yaojun@iet.cn

Abstract: Thermal error is a critical factor limiting the machining accuracy of ultra-precision CNC machine tools. Addressing the issue of weak generalization capability in pure data-driven models under uncalibrated operating conditions due to the lack of physical guidance, this paper proposes a physics-informed "LSTM-PDE" thermal error prediction model for ultra-precision motorized spindles. First, a lumped parameter thermal resistance network (LPTRN) for the motorized spindle is constructed based on heat transfer mechanisms and transformed into state-space equations. This approach achieves millisecond-level rapid calculation of the full-node temperature field, providing an efficient physical benchmark for thermal prediction. Second, a deep learning framework guided by physical priors is constructed, with a re-formulated loss function optimization strategy. By embedding the governing equations of the LPTRN into the neural network as consistency constraints, physical laws are utilized to rectify and guide model weight optimization in real-time. Furthermore, leveraging the advantages of Bi-LSTM in the dynamic compensation of nonlinear residuals, the model corrects systematic biases in traditional mechanistic models arising from rigid constraints and simplified boundary conditions. Experimental results demonstrate that the proposed coupled model effectively resolves prediction distortion under uncalibrated operating conditions. At an unlearned rotational speed of 5500 r/min, the prediction Root Mean Square Error (RMSE) is only 0.03. In the cutting verification of typical feature parts, the model reduced the Z-axis thermal drift error by 72%. This study confirms that the proposed method exhibits both high prediction accuracy and robustness, providing an effective solution for real-time thermal error compensation in ultra-precision machine tools.

Keywords: Ultra-precision Motorized Spindle; Thermal Error Prediction; Thermal Resistance Network; LSTM-PDE

1 Introduction

In ultra-precision machining, although the high power density integration of motorized spindles enhances drive efficiency, the dense internal heat sources and limited heat dissipation induce severe thermo-mechanical coupling effects [1,2]. Studies indicate that thermally induced errors account for 40% to 70% of total machining errors. In particular, the non-uniform temperature rise caused by the superposition of multi-source heat flows during high-speed operation has become a major bottleneck constraining machining accuracy [3,4]. Since structural design cannot completely eliminate thermal deformation, establishing a robust prediction model and implementing real-time compensation is an essential approach to enhancing machine tool performance.

Regarding the thermal error modeling of motorized spindles, data-driven methods, represented by Long Short-Term Memory (LSTM) networks, have become the primary focus of current research in thermal error compensation due to their powerful nonlinear fitting capabilities [5]. Existing studies often further exploit feature potential to improve prediction accuracy by introducing strategies such as attention mechanisms or residual networks [6-8]. However, such pure data-driven models are essentially "black-box" architectures lacking physical interpretability. In actual machining, as it is difficult to cover all variable speed operating conditions, pure data models often exhibit poor generalization ability in uncalibrated regions (unseen conditions) and are susceptible to sensor noise interference, resulting in insufficient robustness of the compensation system.

To overcome the limitations of data-driven models, integrating physical mechanisms as prior knowledge into deep learning architectures has become a research trend for improving model generalization performance. Although the Finite Element Method (FEM) can provide detailed physical field distributions, its high computational cost makes it difficult to meet the requirements for real-time compensation [9,10]. In contrast, the Thermal Resistance Network (TRN) based on the lumped parameter method possesses extremely high computational efficiency [11,12]. However,

traditional TRN models are mostly based on the "free expansion" assumption, ignoring the stiffness constraints generated by bearing preload and housing assembly, thus leading to systemic mechanistic deviations.

In view of this, this paper proposes a physics-informed LSTM-PDE thermal error prediction model, aiming to improve and constrain traditional data-driven methods at the physical level. The model first utilizes a structural stiffness factor to correct the mechanistic deviation of the TRN model, establishing a thermal elongation equation that conforms to real assembly constraints. Subsequently, this equation is embedded into the deep learning architecture as a physical consistency constraint. Through a dual-driven logic of "physical prior guidance + dynamic residual compensation," the training process of the LSTM is made to adhere to thermodynamic laws. The core significance of this work lies in utilizing physical laws to rectify the weight search space of the data model, fundamentally enhancing the model's robustness and generalizability across the full speed range [13,14]. Through multi-condition experiments on an ultra-precision motorized spindle platform, the real-time compensation efficacy of the coupled model under complex thermal environments is verified.

2 Thermal Resistance Network Modeling of Ultra-Precision Motorized Spindles

In this section, a lumped parameter model considering structural stiffness constraints is established by analyzing the heat sources and heat transfer paths of the motorized spindle. By embedding this model as a physical kernel into the LSTM network architecture, a dual-driven prediction framework featuring “physics prior injection” and 'dynamic residual compensation' is constructed.

2.1 Analysis of Heat Sources and Heat Transfer Mechanisms of the Motorized Spindle

During the operation of the motorized spindle, the built-in motor serves as the primary heat source inducing the system's temperature rise. To establish an accurate thermal characteristic model of the motorized spindle, it is necessary to quantitatively calculate its heat generation rate. The heat generation rate represents the heat generated

within a unit volume, and its calculation formula can be expressed as:

$$\bar{q} = \frac{Q}{V} \tag{1-1}$$

$\bar{q}$ is the heat generation rate, W/m^3; Q is the heating power, W; and V is the volume, m^3.

During operation, the built-in motor experiences inherent power losses. These losses, relative to the rated power, are typically converted into heat generated by the stator and rotor[15]. The calculation formula is as follows:

$$P_{loss} = P_e(1 - \eta) \tag{1-2}$$

P_{loss} is the power loss ,W; P_e is the rated power ,W; η is the motor efficiency.

Assuming $\eta = 0.8$, given that the rated power of the motorized spindle in this study is 1170 W, the power loss is calculated to be approximately 234 W. Previous research indicates that during high-speed operation, one-third of the motor's heat (approx. 78 W) is generated by the rotor, while the remaining two-thirds (approx. 156 W) is generated by the stator. The heat generation rates for the stator and rotor are summarized in Table 1-1. Here, d denotes the inner diameter of the stator and rotor, D represents the outer diameter, and L is the length.

Table 1. Heat generation rates and geometric parameters of the stator and rotor.

Component	d/m	D/m	L/m	V/(m^3)	q/($W \cdot m^{-3}$)
Stator	0.069	0.09	0.063	1.65×10^{-4}	9.45×10^{5}
Rotor	0.04	0.067	0.039	8.85×10^{-5}	8.81×10^{5}

During operation, the motorized spindle dissipates heat primarily through the coupling effect of air and cooling water. The internal and external heat transfer processes are governed by conduction, convection, and radiation.

Under high-speed rotation, the convective heat transfer coefficient at the rotor ends is calculated using Equations (1-3) and (1-4):

$$h_1 = 28(1 + \sqrt{0.45u}) \tag{1-3}$$

$$u = \frac{\pi n d}{60} \tag{1-4}$$

h_1 is the convective heat transfer coefficient at the rotor ends, $W/(m^2 \cdot °C)$; u is the

peripheral velocity of the rotor ends, m/s; n is the spindle speed, r/min; and d is the average diameter of the rotor ends, m.

When the rotor rotates, the surface roughness between the stator and the rotor cannot be ignored. Therefore, the heat transfer coefficient between the stator and the rotor can be obtained via Eqs. (1-5)–(1-8) [16]:

$$h_2 = \frac{N_u \lambda}{\delta} \tag{1-5}$$

$$N_u = \frac{0.85\overline{Re}C_{f_1}}{1-\frac{0.953}{\overline{Re}C_{f_1}}} \tag{1-6}$$

$$\overline{Re} = \frac{Re}{1+\sqrt{C_{f_2}/C_{f_1}}} \tag{1-7}$$

$$Re = \frac{u_l \delta}{v_f} \tag{1-8}$$

Where h_2 is the heat transfer coefficient between the stator and rotor ,W/(m^2·K); N_u is the Nusselt number; λ is the thermal conductivity of air ,W/(m·K); δ is the air gap between the stator and rotor ,m; $\overline{Re}$ is the comprehensive Reynolds number; u_l is the air velocity ,m/s; v_f is the kinematic viscosity ,m^2/s; and C_{f_1}, C_{f_2} are the air friction coefficients of the stator and rotor, respectively.

The convective heat transfer coefficient between the cooling jacket and the stator/rotor is generally influenced by fluid properties, flow velocity, channel geometry, and temperature difference. For pipe flow, the Dittus-Boelter correlation can be employed [17,18]:

$$h_3 = \frac{Nu \cdot k}{L_c} \tag{1-9}$$

$$Nu = 0.023 \cdot Re^{0.8} Pr^{0.4} \tag{1-10}$$

$$Pr = \frac{\mu c_p}{k} \tag{1-11}$$

$$Re = \frac{\rho v D}{\mu} \tag{1-12}$$

where h_3 is the heat transfer coefficient between the cooling channel and the stator/rotor ,W/(m^2·K); N_u is the Nusselt number; *Re* is the Reynolds number; Pr is the Prandtl number; D is the diameter of the cooling channel ,m; v is the water flow velocity ,m/s; ρ is the water density ,kg/m^3; μ is the dynamic viscosity of water ,Pa·s;

k is the thermal conductivity of water ,W/m·K; and c_p is the specific heat of water , J/kg·K.

The surface of the motorized spindle housing is stationary and exchanges heat with the surrounding air through convection and radiation. The combined heat transfer coefficient is generally taken as 9.7 W/(m^2·℃).

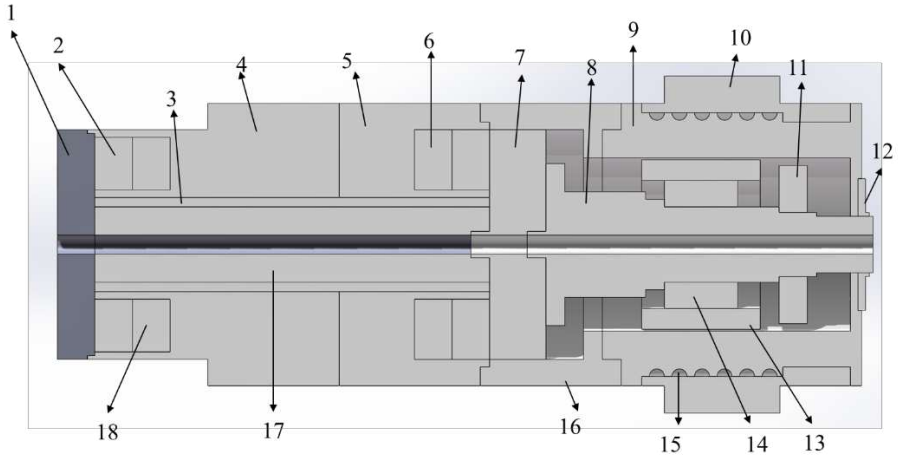
2.2 Rapid Calculation of Motorized Spindle Temperature Field Based on State-Space

2.2.1 Physical Structure and Thermal Network Topological Mapping of the Motorized Spindle

To achieve real-time compensation of thermal errors in ultra-precision machining, it is essential to establish a thermal prediction model that balances computational efficiency with physical fidelity. The research object of this paper is the Huacui UPC200 ultra-precision aerostatic motorized spindle. Its photograph is shown in Fig. 1, and the cross-sectional schematic is illustrated in Fig. 2.



Fig. 1. Photograph of the UPC200 ultra-precision motorized spindle.



1-Upper Thrust Disc 2-Thrust Bearing Stone Grinding Disc 3-Radial Bearing
4-Lower Thrust Bearing Housing 5-Upper Thrust Bearing Housing 6-Lower Thrust Bearing Retaining Plate
7-Lower Thrust Disc 8-Connecting Plate 9-Motor Stator Housing 10-Motor Cooling Jacket
11-Dynamic Balancing Disc 12-Motor Stator Top Cover Stone Grinding Disc 13-Stator
14-Rotor 15-Cooling Water Channel 16-Motor Stator Base 17-Spindle 18-Upper Thrust Disc Retaining Plate

Fig. 2. Cross-sectional view of the UPC200 motorized spindle.

Based on the heat generation mechanisms and heat transfer paths of the motorized spindle, its structure is discretized into 19 key thermal nodes, including the stator, rotor, aerostatic bearings, housing, and cooling circuits, as listed in Table 2. The topological structure of the thermal resistance network constructed based on the lumped parameter method is illustrated in Fig. 3.

Table 2. Node locations and corresponding numbers of the motorized spindle

No.	Location	No.	Location
1	Stator Winding	11	Housing Surface
2	Stator	12	Cooling Channel
3	Rotor Surface	13	Cooling Water Outlet
4	Stator Housing	14	Front End Cap
5	Shaft Front Section	15	Base Contact Point
6	Bearing Interface	16	Rotor End Cap
7	Spindle Nose	17	Shaft Middle Section
8	Bearing Cavity Air	18	Shaft Rear Section
9	Thrust Bearing Zone	19	Ambient Temperature
10	Bearing Housing		

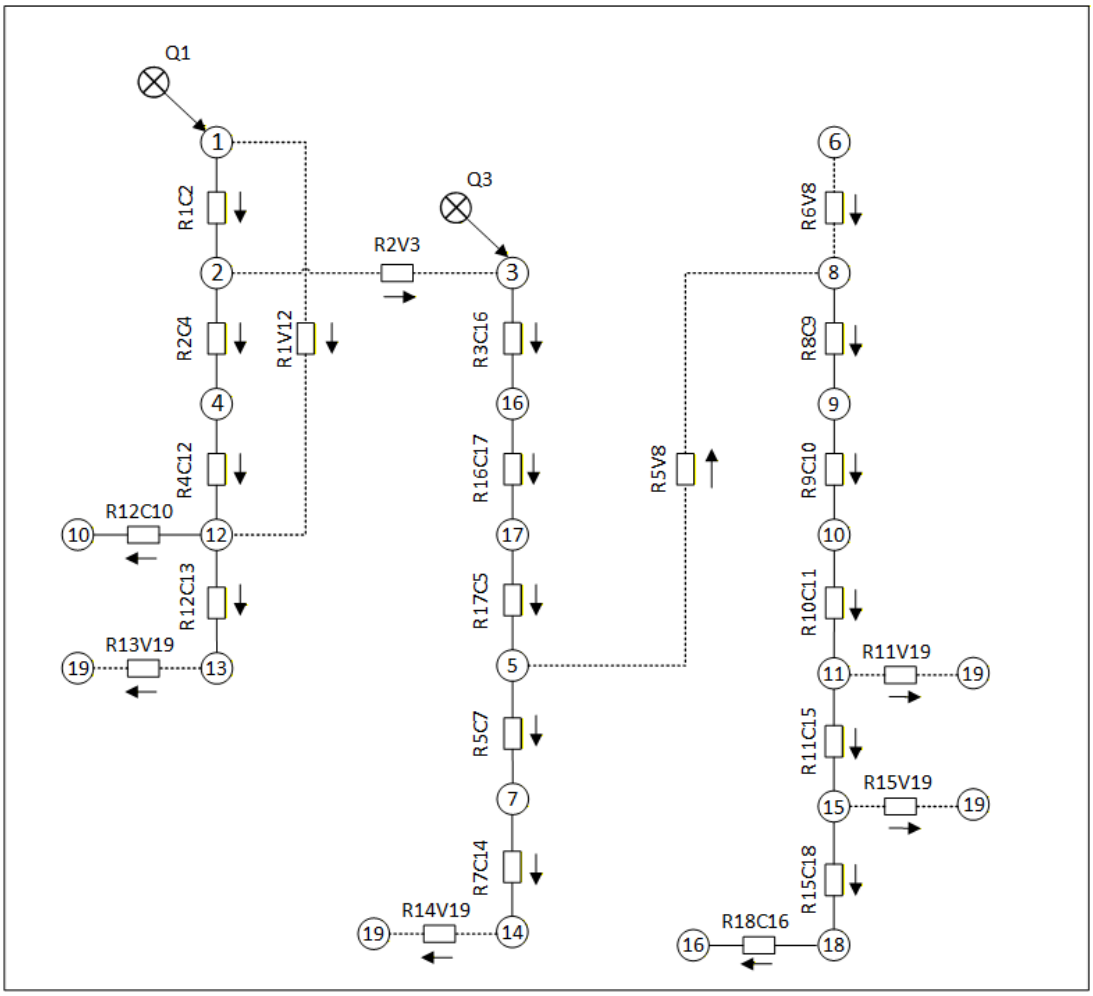


Fig. 3. Topology of the thermal resistance network for the motorized spindle

Here, C denotes conduction, and V denotes convection. Ricj represents the conductive thermal resistance between node i and node j, while Rivj represents the convective thermal resistance between node i and node j. The symbol ⊗ indicates the input heat source, with the heat generation rate of the corresponding node denoted as Q. Arrows indicate the direction of heat flow; solid lines represent conduction, and dashed lines represent convection.

In this network, energy exchange between nodes is governed by the fundamental laws of thermodynamics [19]. The calculation formulas for the internal conductive thermal resistance of solids, surface convective thermal resistance, and contact thermal resistance between assembly interfaces are as follows:

$$R_{cond} = \frac{L}{kA},\ R_{conv} = \frac{1}{hA}, R_{contact} = \frac{1}{h_c A_{contact}}$$

where L is the length of the heat flow path; k is the thermal conductivity of the material; A represents the cross-sectional area or the effective heat transfer area; h is the convective heat transfer coefficient; and h_c is the equivalent contact heat transfer coefficient.

2.2.2 Calculation Results of Key Thermal Parameters of the Motorized Spindle

Considering the complex thermal boundary conditions within the spindle, this paper calculates the thermal resistance values between core components to provide accurate physical parameters for the state-space equations. Fig. 4 illustrates the numerical distribution of key internal thermal resistances of the motorized spindle at 8000 r/min, with the unit of thermal resistance being K/W.

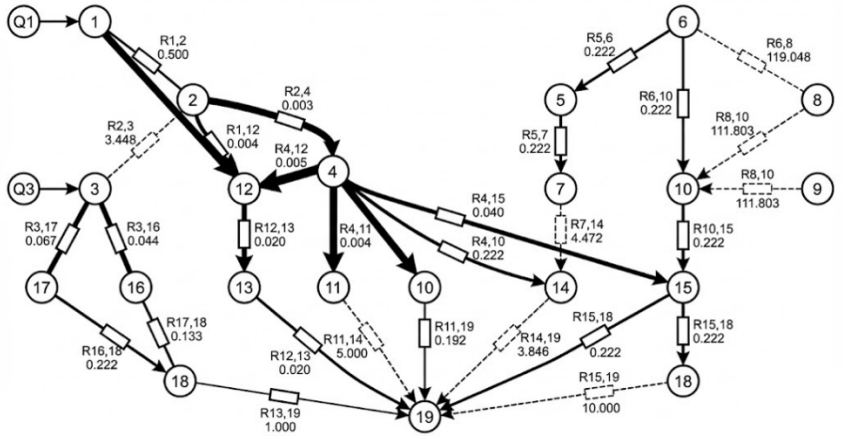


Fig. 4. Calculated thermal resistances of key nodes in the motorized spindle

2.2.3 Formulation and Real-time Solution of the State-Space Equation for the Motorized Spindle

To overcome the efficiency bottlenecks of the traditional Finite Element Method (FEM) in real-time calculation, this paper reconstructs the thermal resistance network into a standard first-order Linear Time-Invariant state-space model based on graph theory topology. According to the law of conservation of energy, the transient thermal balance equations for all key nodes can be expressed in a unified matrix form:

$$\boldsymbol{C}\dot{\boldsymbol{T}}(t) = -\boldsymbol{G}\boldsymbol{T}(t) + \boldsymbol{Q}(t) + \boldsymbol{B}\boldsymbol{U}(t)$$

Where $\boldsymbol{T}(t)\epsilon R^{19}$ is the state vector of transient temperature values containing all key nodes; $\boldsymbol{C}$ is the 19 times 19 heat capacity matrix, reflecting the thermal inertia of various parts of the system; **G** is the symmetric sparse thermal conductance matrix, characterizing the thermal coupling strength between nodes; **Q**(t) is the input heat source vector varying with rotational speed; and $\boldsymbol{U}(t)$ and $\boldsymbol{B}$ are the ambient boundary condition vector and its association matrix, respectively.

To achieve a millisecond-level solution computationally, the thermal balance equation needs to be transformed into the standard state-space equation form $\dot{\boldsymbol{T}} = \boldsymbol{A}\boldsymbol{T} + \boldsymbol{P}$, where the system matrix is $\boldsymbol{A} = -\boldsymbol{C}^{-1}\boldsymbol{G}$ and the input matrix is $\boldsymbol{P} = \boldsymbol{C}^{-1}(\boldsymbol{Q} + \boldsymbol{B}\boldsymbol{U})$. For this first-order stiff system of ordinary differential equations , this paper employs the fourth-order Runge-Kutta algorithm for explicit discrete solution. Its time-domain recursive scheme is as follows:

$$\boldsymbol{T}_{k+1} = \boldsymbol{T}_k + \frac{h}{6}(\boldsymbol{K}_1 + 2\boldsymbol{K}_2 + 2\boldsymbol{K}_3 + \boldsymbol{K}_4)$$

$$s.t.\begin{cases} \boldsymbol{K}_1 = f(t_k, \boldsymbol{T}_k) \\ \boldsymbol{K}_2 = f\left(t_k + \frac{h}{2}, \boldsymbol{T}_k + \frac{h}{2}\boldsymbol{K}_1\right) \\ \cdots \end{cases}$$

Where h is the integration step size (set as h=0.01s in this paper). In contrast to Finite Element Analysis (FEA), which requires handling tens of thousands of degrees of freedom and nonlinear iterations, the proposed state-space model leverages the parallelism of matrix operations to reduce the single-step temperature field solution time to less than 10ms. This rapid calculation mechanism not only enables real-time response to thermal field fluctuations induced by sudden changes in spindle speed but also provides a high-frequency, low-latency physical prior data stream interface for the subsequent neural network model.

2.2.4 Accuracy Validation of the Thermal Resistance Network Model for the Motorized Spindle

To validate the accuracy of the rapid calculation model, a temperature rise comparison experiment was conducted under the operating condition of 8000 r/min. The front end cap (Node 7) and the spindle housing (Node 11) were selected as observation points. The comparison between the calculated results of the thermal network model and the measured temperature curves is illustrated in Fig. 5.

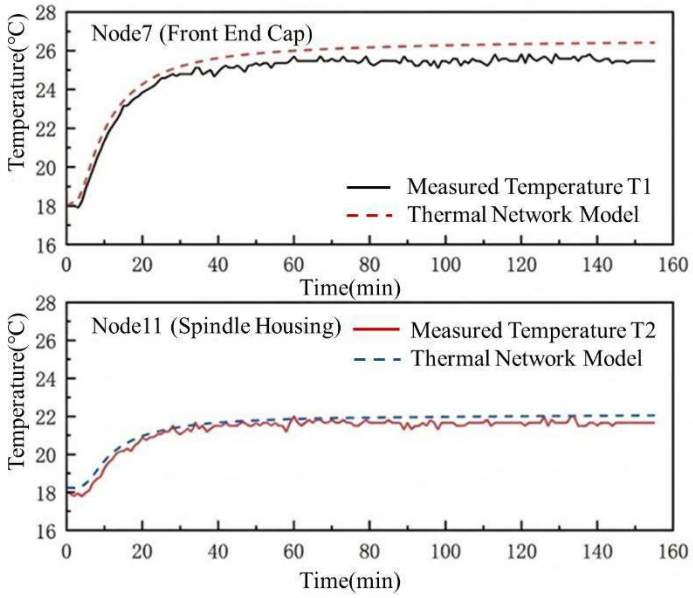


Fig. 5. Comparison between the calculated results of the thermal network model and the measured temperature curves

The results indicate that the prediction errors of the TRN model during the steady-state phase are consistently within 5%, and the transient response trends show high agreement with the measured data. This demonstrates that the constructed rapid calculation model possesses high physical fidelity while ensuring real-time performance, making it suitable as a physical constraint benchmark for the Bi-LSTM

model.

2.3 Framework of the LSTM-PDE Thermal Error Prediction Model

To overcome the limitations of parameter sensitivity in mechanism models and the dependence on massive samples in data-driven models, this section proposes an LSTM-PDE prediction framework. By incorporating the modified thermal resistance network as a physical constraint into the loss function of the Bi-LSTM, the framework achieves precise mapping of nonlinear thermal errors guided by physical laws. The flowchart of this framework is illustrated in Fig. 6.

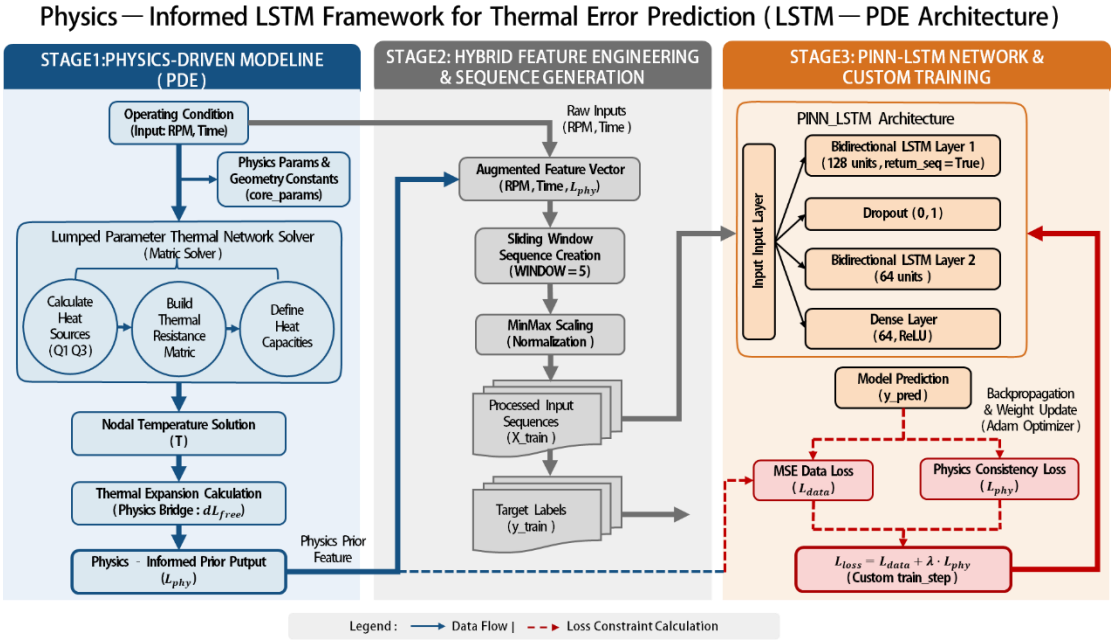


Fig. 6. Flowchart of the proposed LSTM-PDE thermal error prediction framework

2.3.1 Physical Prior Feature Extraction and Input Enhancement

To enhance the prediction robustness of the model across the full speed range, this paper establishes prior features based on physical mechanisms, directly incorporating the thermal dynamic behaviors of the motorized spindle into the model. The specific process is as follows:

1.Dynamic Condition Simulation and Numerical Solution: A random sampling strategy is adopted within the full operating range of 0–8000 r/min to generate rotational speed sequences. The fourth-order Runge-Kutta method is utilized to perform numerical discretization on the thermal state-space equations comprising 19 nodes. This process captures the temperature rise lag effect induced by heat capacity, thereby obtaining a high-resolution transient physical dataset.

2.Structural Stiffness Constraint Mapping: To address the "mechanism bias" caused by traditional models ignoring mechanical constraints, a stiffness correction model is embedded during the data generation phase. By introducing a stiffness coupling factor η, the free expansion displacement is mapped to the actual thermal

elongation subject to the equivalent constraints of the bearings and base. The physical ground truth is defined as $E(t) = \eta \cdot \Delta L(t)$.

3.Input Feature Reconstruction and Injection: In the input layer, in addition to rotational speed and time loads, the physical prior displacement calculated by the modified mechanism model is explicitly injected. Through sliding window technology, multi-dimensional sequences are transformed into tensor inputs. This endows the neural network with the capability to perceive heat conduction laws right at the input stage, thereby effectively converging the model's weight search space under the guidance of physical prior features.

2.3.2 Design of the Bi-directional Long Short-Term Memory Network Topological Architecture

Given the significant time lag and cumulative effects of thermal errors in motorized spindles, this paper adopts the Bi-directional Long Short-Term Memory network (Bi-LSTM) as the core predictor. By synchronously extracting information on historical thermal load evolution and future trend constraints, it enhances the model's capability to capture nonlinear thermal behaviors [20-22].

A deep learning prediction system was constructed based on the TensorFlow framework, achieving in-depth extraction of thermal characteristics through a multi-layer architecture. First, in the temporal reconstruction layer, a sliding window technique (w=5) is employed to map external loads and physical prior features into high-dimensional tensors, ensuring the model captures the local evolution laws of heat flow gradients. The core computation layer consists of a Bi-LSTM network: the first layer is configured with 128 hidden units, synchronously extracting dynamic features of heat generation accumulation and heat dissipation through forward and backward dual channels; the second layer is configured with 64 hidden units, utilized for nonlinear manifold compression of high-dimensional features to further extract deep semantic information related to thermal elongation. To enhance the generalization and robustness of the model, a Dropout regularization mechanism (p=0.05) is introduced between network layers. By randomly dropping out neurons, this mechanism suppresses overfitting to the physically generated data and simulates sensor signal noise. Finally, in the regression output layer, a fully connected layer combined with a linear activation function is used to map the extracted hierarchical features to the final predicted value of the axial thermal error.

2.3.3 Coupled Driving and Intelligent Calibration Under Physics-Consistent Loss Constraints

To address the issues of physical uninterpretability and poor generalization capabilities under uncalibrated operating conditions inherent in purely data-driven models, this paper proposes a loss function reconstruction strategy based on physical

consistency. Unlike traditional deep learning approaches that solely aim to minimize prediction errors, this model introduces thermodynamic governing equations as hard constraints during the training phase.

The total loss function of the system is defined as a weighted combination of the data fitting term and the physical residual term:

$$L_{loss} = L_{data} + \lambda \cdot L_{phy}$$

Where λ is the physical constraint weighting coefficient, used to balance the relative contributions of the data-driven and mechanism-guided components; L_{data} is the data-driven loss term, which employs the Mean Squared Error (MSE) to quantify the deviation between the thermal error values predicted by the neural network and the measured ground truth from sensors, ensuring the model possesses basic fitting capability; and L_{phy} is the physical residual loss term, defined as the thermodynamic derivative constraint:

$$L_{phy} = \left\| \frac{\partial \boldsymbol{E}_{NN}}{\partial t} - \boldsymbol{T}_t \cdot (\boldsymbol{AT} + \boldsymbol{P}) \right\|^2$$

This term ensures that the dynamic response characteristics of the network predictions are strictly governed by the heat conduction mechanism by constraining the non-physical deviation between the neural network output gradients and the theoretical temperature rise rates calculated from the state-space equations. Consequently, it eliminates “high-frequency artifacts” or “trend drifts” that may arise in purely data-driven models.

Under the aforementioned physical constraints, the Bi-LSTM network is no longer required to learn the complete “speed-thermal error” mapping; instead, it focuses on capturing the residual components resulting from the simplification of the mechanism model. Based on the dual mechanism of physical constraints and residual compensation, this model embeds the laws of thermodynamics conservation as a regularization term within the deep learning framework. This strategy, while ensuring that the model output strictly adheres to physical evolution laws, effectively enhances its capability to dynamically capture minute error fluctuations under time-varying thermal boundary conditions.

3 Experimental Setup and Model Calibration

To reveal the temperature evolution laws and thermal deformation mechanisms of the motorized spindle in ultra-precision machine tools, a testing platform for temperature rise and thermal error was established. Through experiments under multiple operating conditions, data regarding the temperature field and thermal elongation of the spindle system during dynamic processes were collected. The experimental scheme encompasses basic operating condition experiments for model

parameter calibration, as well as online machining compensation verification realized through the cutting of 'double-arc' and “double-plane” test pieces. The aim is to comprehensively evaluate the performance of the LSTM-PDE model from the dual dimensions of modeling accuracy and machining quality.

3.1 Construction of the Thermal Characteristic Testing Platform for the Ultra-Precision Motorized Spindle

The experiments were conducted on the Huacui UPC200 ultra-precision hydrostatic motorized spindle platform. The spindle is directly driven by a built-in torque motor, with a maximum rotational speed of 8000 r/min. To eliminate the influence of environmental thermal disturbances on ultra-precision machining accuracy, the experiments were carried out in a constant temperature clean room at 20±0.5℃. The spindle cooling system employed a constant temperature liquid chiller set at 18℃. The configuration of the experimental platform is illustrated in Fig. 7.

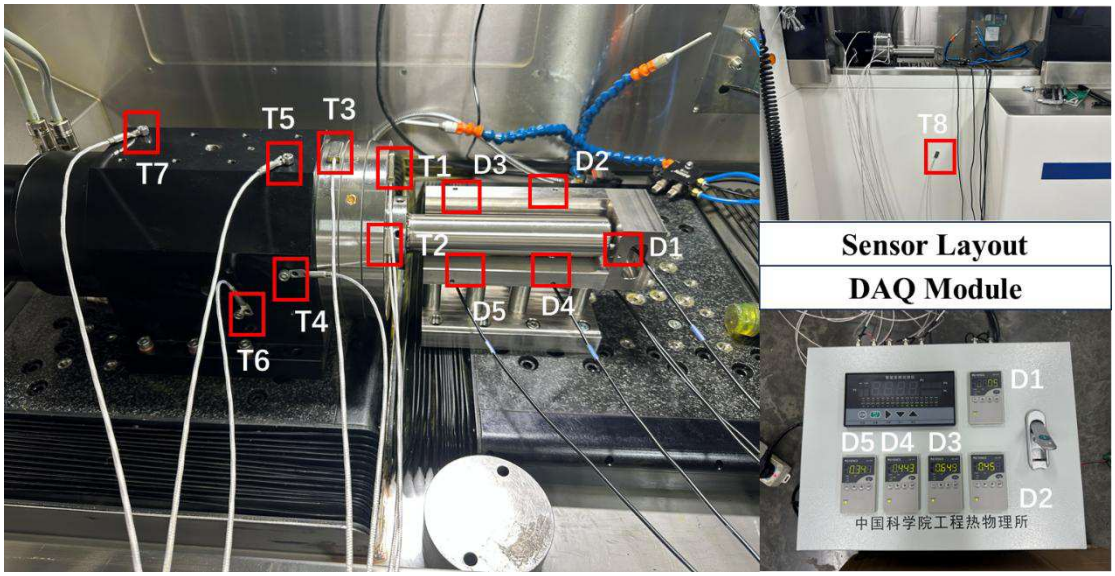


Fig. 7. Measurement system for temperature rise and thermal error of the motorized spindle

The temperature field of the spindle is monitored in real time by eight PT100 sensors, the spatial distribution of which is detailed in Table 3. The axial and radial thermal displacements of the spindle are acquired by five eddy current displacement sensors. All signals are synchronously collected via a data acquisition card and then displayed and stored in real time by self-developed host computer software.

Table 3. Distribution of temperature sensors on the motorized spindle

Sensor No.	Sensor Location
#1,2	Spindle end face
#3	Spindle annular face
#4-7	Spindle housing

#8	Machine tool body

3.2 Training Set Experiments: Tests under Multi-speed Operating Conditions

In view of the nonlinear evolution laws of the thermal characteristics of the motorized spindle varying with rotational speed, thermal error experiments under multiple sets of typical rotational speed operating conditions were designed and conducted in this paper. The study aims to reveal the temperature rise evolution laws and thermal response characteristics of the system under variable speed conditions.

Table 4. Experimental operating conditions for the thermal characteristics of the motorized spindle

Exp. No.	Motor Speed (r/min)	Operation Mode
#1	1500	Constant speed rotation for 120 min
#2	3000	Constant speed rotation for 120 min
#3	4500	Constant speed rotation for 120 min
#4	6000	Constant speed rotation for 120 min
#5	8000	Constant speed rotation for 120 min

Five sets of constant-speed experiments ranging from 1500 to 8000 r/min were set up (detailed in Table 4). Each operating condition was maintained for 120 min with a sampling interval of 1 min to acquire stable thermal characteristic data.

3.3 Generalization Performance Verification Experiment I: Multi-speed Tests

To verify the generalization capability of the model across the full speed range, four typical rotational speed points excluded from the training set were selected for comparative experiments in this section (detailed in Table 5). The experiments were maintained for 120 min with a sampling interval of 1 min, aiming to evaluate the prediction robustness of the model against completely unseen operating conditions.

Table 5. Experimental operating conditions for the thermal characteristics of the motorized spindle

Exp. No.	Motor Speed (r/min)	Operation Mode
#1	2500	Constant speed rotation for 120 min
#2	4000	Constant speed rotation for 120 min
#3	5500	Constant speed rotation for 120 min
#4	7000	Constant speed rotation for 120 min

If the model merely “memorized” the training data, prediction deviations or oscillations would inevitably occur at these intermediate speed points. Conversely, if the predicted curves show high agreement with the measured curves, it serves as strong evidence that the LSTM-PDE architecture has successfully learned the physical mapping mechanism between rotational speed and thermal error.

3.4 Generalization Performance Verification Experiment II: Cutting of Test Pieces with Typical Features

To verify the online compensation efficacy of the LSTM-PDE model under complex operating conditions such as cutting loads and coolant disturbances, this paper designed a verification experiment using aluminum alloy test pieces containing “reference plane + large-radius arc” features.

3.4.1 Test Piece Design and Experimental Procedure

The test piece adopts a combined structure of an R200 mm large-radius arc and a top reference plane, designed to enhance the sensitivity to profile error by utilizing large-radius curved features.The experiment adopts a “1+2” comparison mode: under unified operating conditions of rotational speed n=5000 r/min, feed rate f=1 mm/min, and depth of cut a_p=0.02mm, one benchmark workpiece without compensation (in the thermal state) and two workpieces with LSTM-PDE real-time compensation enabled were machined sequentially. The compensation system synchronously collects temperatures at a frequency of 1 Hz and dynamically corrects the Z-axis coordinate through the CNC external zero offset interface, in order to verify the correction accuracy and machining consistency of the algorithm.

3.4.2 Evaluation Metrics and Inspection

Upon completion of the experiments, the test pieces were inspected using an ultra-precision profilometer to establish a dual-dimensional evaluation system based on the axial thermal drift error (denoted as ΔZ) and the arc profile error (denoted as P_t).Specifically, ΔZ takes the height of the workpiece in the cold state as the reference, aiming to quantify the model's suppression capability against Z-axis zero-point thermal drift and the error reduction rate.Meanwhile, P_t evaluates the correction performance of the model during the dynamic interpolation process by measuring the maximum normal deviation of the actual profile of the R200 mm arc segment relative to the ideal geometric trajectory. Furthermore, combined with the consistency performance of consecutively machined workpieces, it verifies the engineering robustness of the algorithm under long-term operation."

4 Results and Discussion

Based on the ultra-precision motorized spindle testing platform and the machining scheme for typical test pieces, this section quantitatively evaluates the performance of the LSTM-PDE coupled model from three dimensions: basic thermal characteristics, model generalization accuracy, and online compensation efficacy. The analysis process follows the progressive logic of “thermal characteristic unveiling—full-speed range generalization verification — verification through actual machining”, aiming to

comprehensively validate the robustness of the proposed method under uncalibrated operating conditions and its engineering application value in the field of precision machining.

4.1 Analysis of Thermal Dynamic Characteristics of the Motorized Spindle Over the Full Speed Range

To investigate the evolution laws of the thermal field of the motorized spindle across the full speed range, this section analyzes data from five sets of basic operating conditions within the range of 1500-8000 r/min. In response to displacement fluctuations caused by environmental noise, signal interference, and machine tool vibration during the data acquisition process, noise reduction preprocessing was performed on the data using outlier removal and smoothing filtering algorithms. The dynamic response of the temperature at each monitoring point varying with rotational speed is illustrated in Fig. 8.

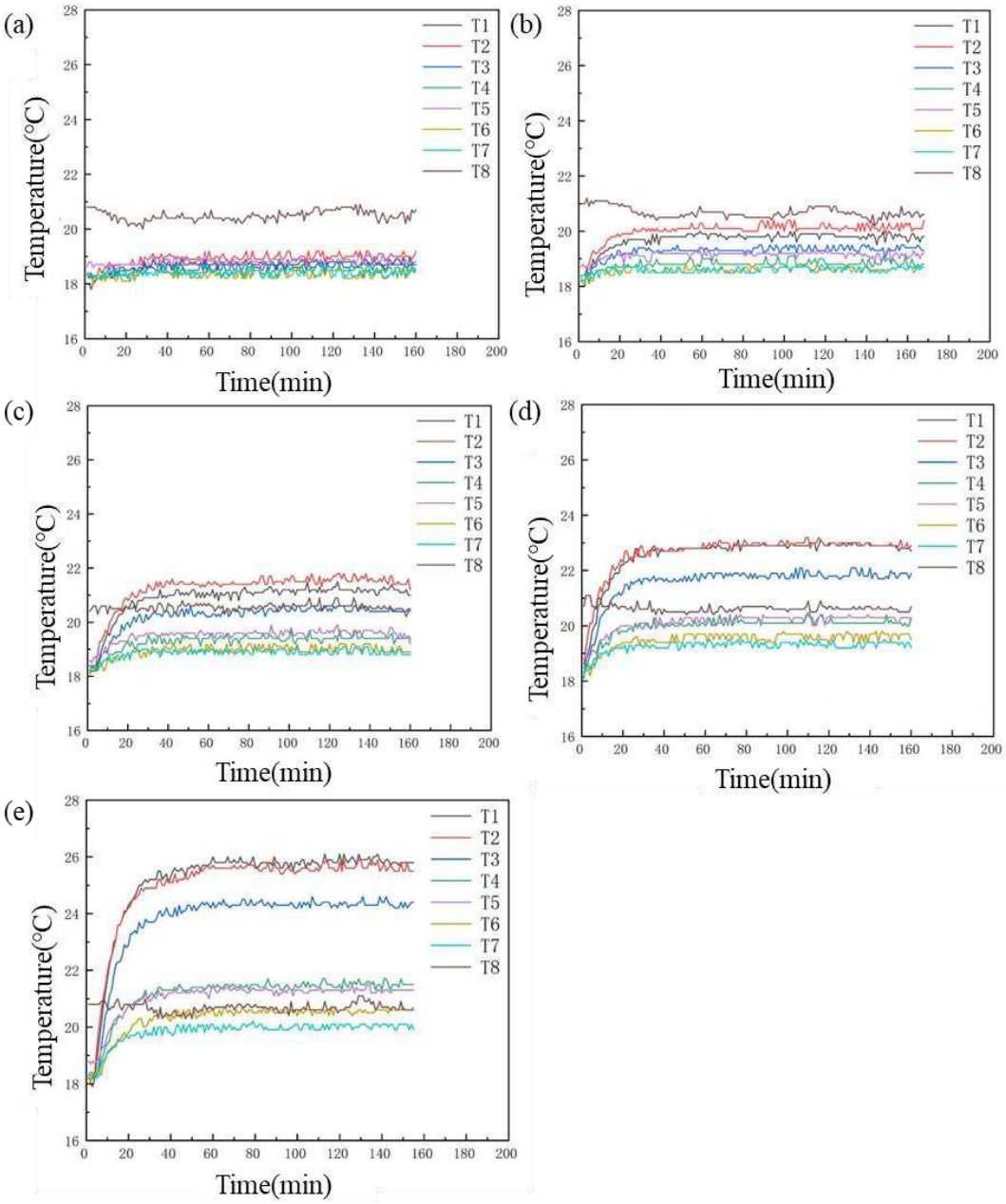


Fig. 8. Temperature curves of the motorized spindle under various rotational speeds: (a) 1500 r/min; (b) 3000 r/min; (c) 4500 r/min; (d) 6000 r/min; (e) 8000 r/min.

Fig. 8 indicates that the temperature rise at each monitoring point exhibits a distinct non-linear positive correlation with increasing rotational speed. Influenced by the sensor locations and their proximity to the heat source, the temperature rise at point T1, located nearest to the spindle center, is the most significant, followed by T2 and T3. When the rotational speed exceeds 4500 r/min, the sensitivity of the temperature rise to changes in speed increases substantially. Furthermore, the time required for the system to reach thermal equilibrium significantly shortens as the thermal load intensifies.

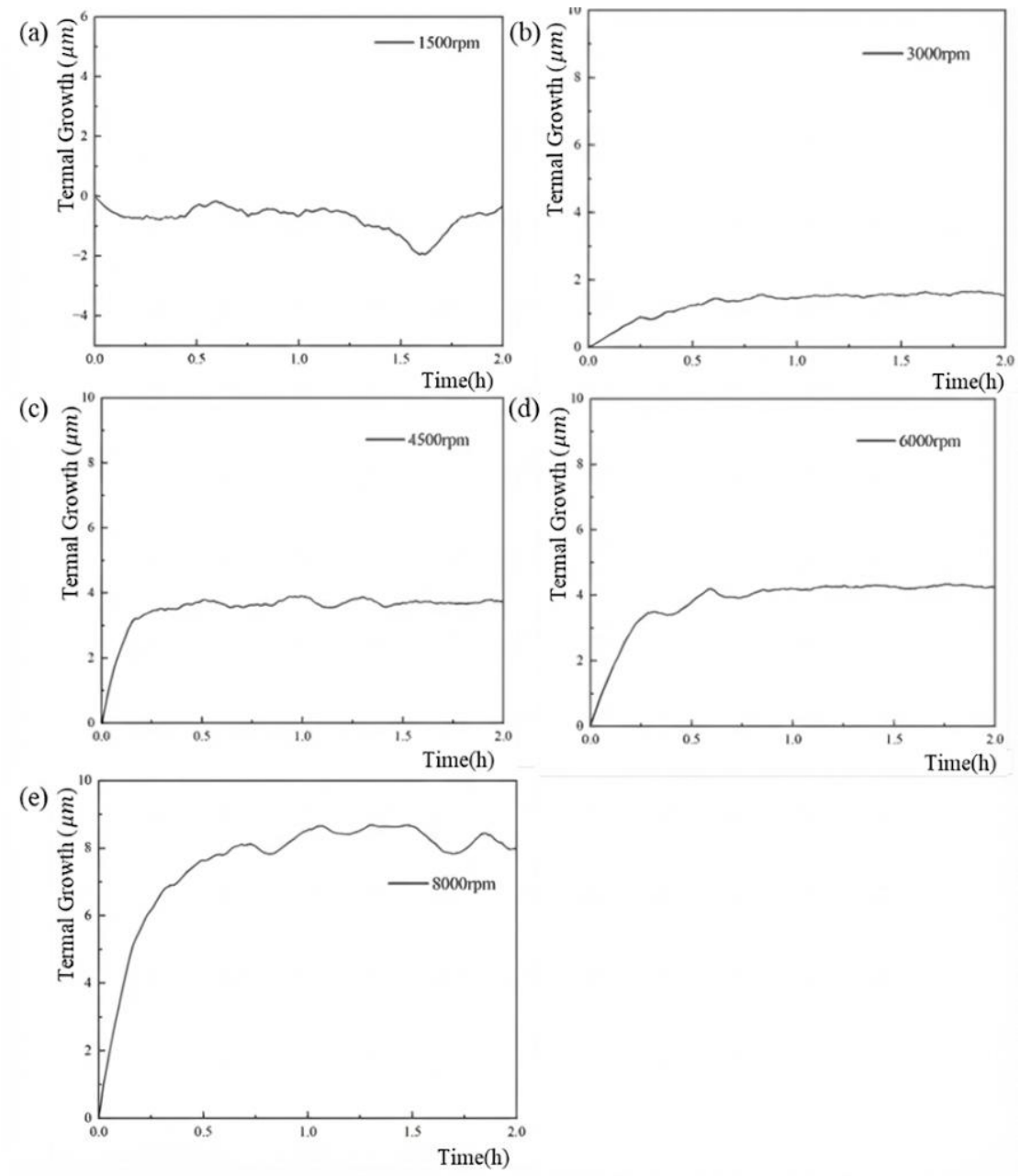


Fig. 9. Axial thermal elongation curves of the motorized spindle under various rotational speeds: (a) 1500 r/min; (b) 3000 r/min; (c) 4500 r/min; (d) 6000 r/min; (e) 8000 r/min.

Fig. 9 illustrates the evolution curves of thermal elongation under different rotational speeds, where all operating conditions exhibit a distinct exponential characteristic of "rapid rise–stabilization". By performing exponential fitting on the raw data, not only was random noise effectively smoothed out, but the system's thermal response speed and steady-state elongation were also quantified. The analysis reveals that the spindle thermal elongation increases nonlinearly with the rotational speed: the growth is relatively slow below 4500 r/min; however, exceeding this threshold, influenced by the drastic increase in frictional heat generation, both the thermal elongation magnitude and the evolution rate rise substantially, reaching a maximum

value (approximately $8\,\mu m$) at 8000 r/min. This provides a quantified physical benchmark for the subsequent prediction model.

4.2 Generalization Performance Evaluation of the LSTM-PDE Model

After completing the model calibration using five sets of basic operating conditions within the 1500–8000 r/min range, to further evaluate its generalization performance under unspecified continuous operating conditions, this section introduces four sets of completely independent validation sets for 'blind testing'. By analyzing the temperature rise response (Fig. 10) and thermal elongation curves (Fig. 11) under the validation conditions, the prediction robustness of the model against unseen operating conditions is rigorously assessed from two dimensions: steady-state interpolation accuracy and transient tracking capability.

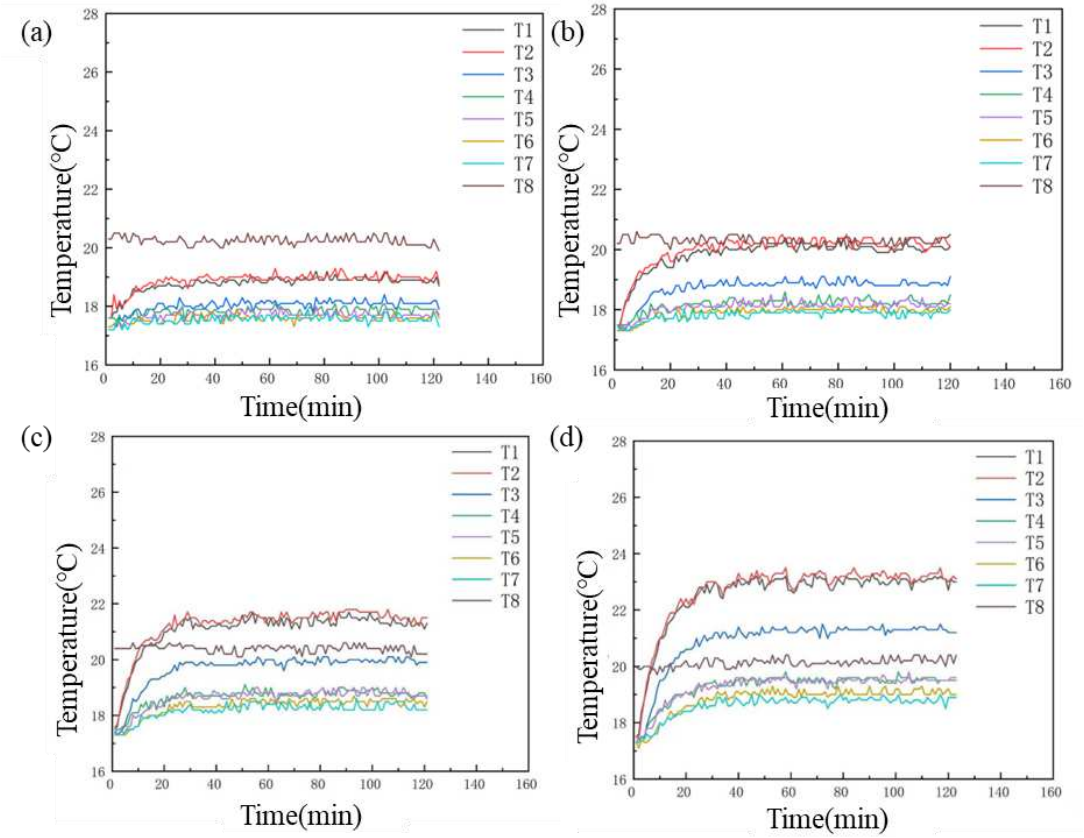


Fig. 10. Temperature curves of the motorized spindle under various rotational speeds: (a) 2500 r/min; (b) 4000 r/min; (c) 5500 r/min; (d) 7000 r/min.

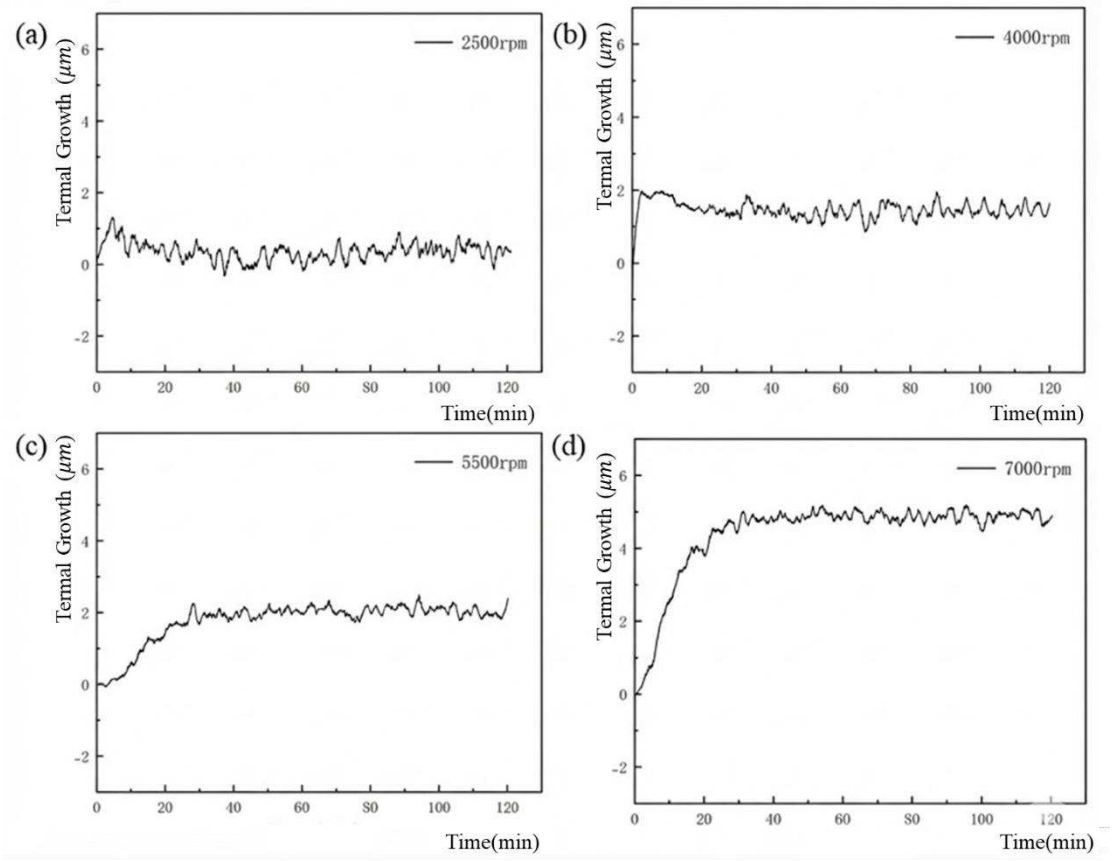


Fig. 11. Axial thermal elongation curves of the motorized spindle under various rotational speeds: (a) 2500 r/min; (b) 4000 r/min; (c) 5500 r/min; (d) 7000 r/min.

In terms of steady-state prediction, the LSTM-PDE model effectively corrects the interpolation distortion often observed in traditional data-driven methods under uncalibrated operating conditions.Taking the 5500 r/min condition (outside the training range) as an example, the pure LSTM model, influenced by strong nonlinear factors such as oil film shear heat generation, exhibits significant deviation during the thermal equilibrium stage, with a maximum absolute error reaching 2.4μm (RMSE = 1.24).In contrast, by incorporating thermal resistance network equations as physical constraints, the LSTM-PDE model forces the output to comply with thermodynamic evolution laws, achieving precise guidance of the solution space.Quantitative analysis reveals that the prediction RMSE of the coupled model under this condition is controlled within 0.03, representing an accuracy improvement of approximately 97% compared to the pure data-driven model.This comparison confirms that the incorporation of physical priors enables the model to internalize the thermal-mechanical coupling mechanism across the full speed range, thereby possessing stronger cross-condition generalization capability.

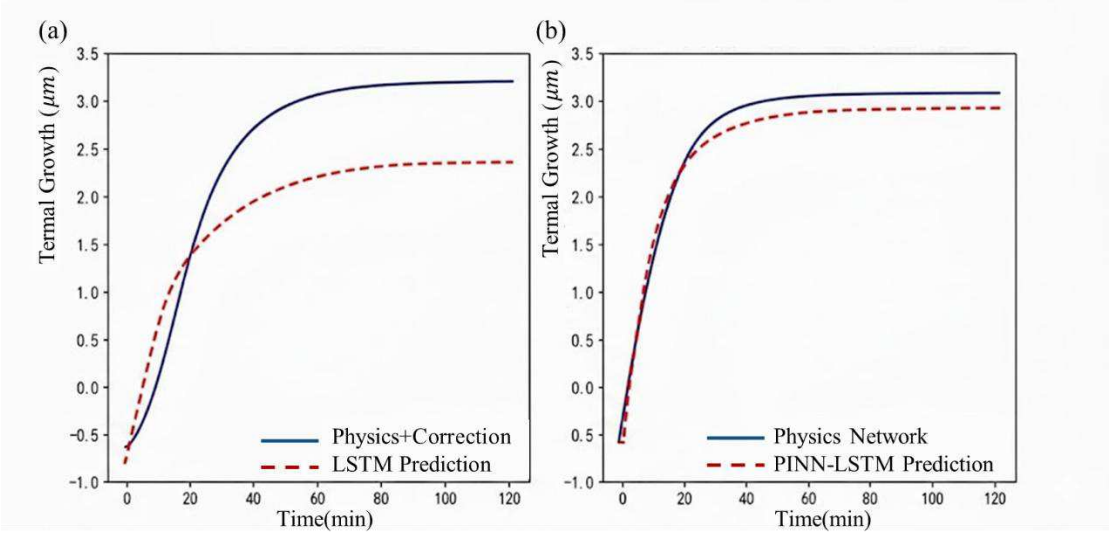


Fig. 12. Comparison of model prediction performance under the validation operating condition of 5500 r/min: (a) Prediction data of the LSTM model; (b) Prediction data of the LSTM-PDE model.

In terms of transient response, the LSTM-PDE model demonstrates superior dynamic robustness during cold startup and the initial stage of thermal accumulation. As illustrated in Fig. 12, during the startup phase (0–40 min) characterized by drastic temperature rise, traditional data-driven models are affected by the time lag of heat conduction, suffering from severe 'phase lag', which results in significant transient residuals. In contrast, by integrating the temporal memory effect of Bi-LSTM with the energy conservation constraints of physical equations, the LSTM-PDE model can precisely capture the steep rising trend of thermal elongation, effectively resolving the issue of response hysteresis. Under the high-energy state condition of 7000 r/min, which approaches the training boundary, benefiting from the effective compression of the solution space by physical constraints, the 95% confidence interval of the prediction residuals remains consistently within an extremely narrow range, with no physical distortion observed. Synthesizing the steady-state and transient performances, it is confirmed that the proposed coupled model possesses excellent physical generalization capability and engineering reliability under complex variable operating conditions.

4.3 Experimental Verification via Cutting of Test Pieces with Typical Features

To evaluate the compensation efficacy of the model in actual machining, surface topography inspections were conducted on the 'cold-state benchmark' test piece, the 'thermal-state uncompensated' test piece, and two consecutive sets of 'thermal-state compensated' test pieces.As shown in Fig. 13, the inspection process was conducted using a Mitutoyo CV-3200 ultra-precision profilometer with a measurement accuracy of $0.1\,\mu m$, aiming to intuitively compare the improvement effect of the model on machining accuracy. Fig. 14 presents the schematic diagram of the inspection process

using the ultra-precision profilometer and the corresponding inspection results.



Fig. 13. Mitutoyo CV-3200 ultra-precision profilometer.

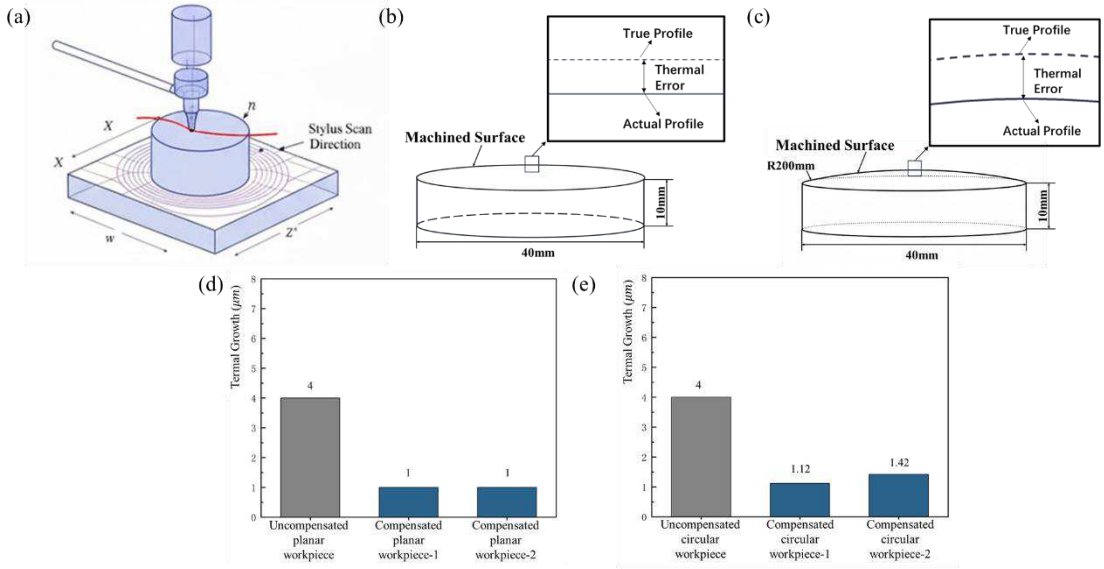


Fig. 14. (a) Schematic diagram of the inspection process; (b) Schematic of the planar workpiece; (c) Schematic of the arc surface workpiece; (d) Error comparison of the machined planar surface; (e) Error comparison of the machined arc surface.

Fig. 14 illustrates the measurement comparison of the R200 arc profile error and axial accuracy for each workpiece. In the uncompensated state, affected by the thermal accumulation at 5000 r/min, the Z-axis generated a thermal drift of approximately $4\mu m$. Upon activating the LSTM-PDE compensation system, the axial thermal drift of the first workpiece decreased to $1.12\mu m$, achieving an error correction rate of 72%. The second consecutively machined compensated workpiece exhibited extremely high consistency, with a deviation of only $0.3\mu m$ from the first piece. These results strongly validate the superior performance of the LSTM-PDE model in counteracting thermal disturbances, suppressing cumulative errors, and ensuring long-term machining stability, thereby meeting the requirements of ultra-precision machining.

The planar cutting experiment aims to exclude interference from multi-axis linkage and purely evaluate the model's compensation capability for Z-axis linear thermal elongation. in ultra-precision machining, this thermal elongation directly manifests as the axial drift of the end-face origin. Fig. 14 presents the comparison of the axial height deviation of each workpiece plane relative to the reference plane. Without compensation, influenced by frictional heat and temperature rise, the spindle generated a systematic axial drift of approximately $4\,\mu m$, resulting in severe dimensional out-of-tolerance. After activating the LSTM-PDE compensation system, the model dynamically corrected the Z-axis coordinates based on the real-time temperature field, significantly causing the axial height deviation to converge to $1\mu m$, with an error correction rate of 75%. The experimental results deeply verify the necessity of introducing the 'stiffness coupling factor' into the model as a physical constraint: compared to the traditional ideal constraint of free expansion, embedding the actual stiffness constraint effectively avoids “numerical overshoot” caused by “over-compensation”. The minimal compensation residual strongly proves that the model can not only accurately capture the thermal-mechanical coupling laws under complex operating conditions but also that its characterization of the spindle's real stiffness constraints highly aligns with the engineering reality of precision machining.

5 Conclution

To address the common issues of the difficulty in establishing mechanistic models and the weak generalization capability of data-driven models in the thermal error prediction of motorized spindles, this paper proposes an LSTM-PDE prediction method based on physics-informed deep learning. The conclusions are as follows:

The deep fusion of physical laws and data features significantly improves prediction accuracy. By constructing a 19-node lumped parameter thermal resistance network for the motorized spindle and converting it into state-space equations, this paper achieved millisecond-level rapid calculation of the full-node temperature field. On this basis, by reconstructing the loss function, the heat transfer governing equations were embedded as explicit constraints into the neural network training, utilizing physical residuals for the real-time correction of model weights. Experiments indicate that this method effectively eliminates the physical distortion inherent in pure data-driven models and successfully captures the complex non-linear thermal behavior of the motorized spindle over the full speed range. In the 5000 r/min cutting validation, the model reduced the axial drift from $4\mu m$ in the uncompensated state to $1.24\mu m$, achieving an error correction rate of 72% and significantly enhancing machining accuracy.

The enhancement of physical priors confers superior robustness and high generalization performance to the model. By embedding physical equations, the LSTM-

PDE architecture ensures that model predictions consistently adhere to fundamental physical principles. At the unseen validation point of 5500 r/min, leveraging the continuity constraints of the physical layer, the prediction Root Mean Square Error (RMSE) was reduced from $1.24\mu m$ (pure data-driven model) to $0.03\mu m$, representing an accuracy improvement of 97%. In terms of transient tracking, the model eliminated the response hysteresis observed in traditional methods; in continuous machining experiments, the dimensional variation between compensated workpieces was merely $0.3\mu m$. The study confirms that by introducing physical equations as constraints, the model not only eliminates response hysteresis in transient tracking but also effectively withstands random disturbances such as sensor noise, ensuring long-term stability and cross-condition generalization capability in complex machining environments.

In summary, the physics-data dual-driven coupled method proposed in this paper, by embedding thermodynamic constraints into the deep learning architecture, resolves the 'black box' problem inherent in pure data-driven models for thermal error prediction from a mechanistic perspective. This method not only demonstrates superior prediction accuracy and physical stability under complex variable operating conditions but also achieves a balance between computational efficiency and model robustness. Consequently, it provides a solid theoretical basis and an engineering solution for the intelligent thermal error control of ultra-precision machine tools across the full speed range.

Declarations

Funding The authors declare that no funds, grants, or other support were received during the preparation of this manuscript.

Competing Interests The authors have no relevant financial or non-financial interests to disclose.

Author Contributions All authors contributed to the study conception and design. Material preparation, data collection and analysis were performed by Yuqing Tang, Hao Zhong, Jun Yao, and Shuai Su. The first draft of the manuscript was written by Yuqing Tang and all authors commented on previous versions of the manuscript. All authors have read and approved the final manuscript.

Availability of Data and Materials The data that support the findings of this study are not publicly available due to commercial confidentiality but are available from the corresponding author or the first author on reasonable request.

References

[1] Ramesh R, Mannan M A, Poo A N. Error compensation in machine tools—a review: part I: geometric, cutting-force induced and fixture-dependent errors[J]. International Journal of Machine Tools and Manufacture, 2000, 40(9): 1235-1256.

[2] Ramesh R, Mannan M A, Poo A N. Error compensation in machine tools—a review: Part II: thermal errors[J]. International Journal of Machine Tools and Manufacture, 2000, 40(9): 1257-1284.

[3] LI Y, YU M L, BAI Y M, et al. A review of thermal error modeling methods for machine tools[J]. Applied sciences, 2021, 11(11): 5216.

[4] Bryan J. International status of thermal error research (1990)[J]. CIRP annals, 1990, 39(2): 645-656.

[5] Coelho C, Hohmann M, Fernández D, et al. Data-Driven Temperature Modelling of Machine Tools by Neural Networks: A Benchmark[J]. arXiv preprint arXiv:2510.03261, 2025.

[6] Lu Q, Zhu D, Wang M, et al. Digital twin-driven thermal error prediction for CNC machine tool spindle[J]. Lubricants, 2023, 11(5): 219.

[7] Chen X, Chen G, Sun Y. Research on thermal error modeling of machine tool electric spindle based on SSA-NAR-LSTM[J]. Proceedings of the Institution of Mechanical Engineers, Part C: Journal of Mechanical Engineering Science, 2025: 09544062251409877.

[8] Li Z, Li G, Xu K, et al. Data-driven thermal error prediction of spindle with mechanism-reinforced temperature information[J]. Advanced Engineering Informatics, 2025, 64: 103005.

[9] Mayr J, Jedrzejewski J, Uhlmann E, et al. Thermal issues in machine tools[J]. CIRP annals, 2012, 61(2): 771-791.

[10] Yu, Haoyang; Gao, Mingming; Zhang, Hongfu; Chen, Jiyu; Liu, Jizhen; Yue, Guangxi; Dynamic Modeling of Key Operating Parameters for Supercritical Circulating Fluidized Bed Units based on Data-Knowledge-Driven Method. Journal of Thermal Science, 2024, 33(3): 1216-1230. http://dx.doi.org/10.1007/s11630-024-1935-y

[11] DEMETRIADES G D，PARRAH Z，ANDERSSON E，et al． A real-time thermal model of a permanent-magnet synchronous motor［J］． IEEE Transactions on Power Electronics，2010，25(2) : 463．

[12] Brecher, C.; Shneor, Y.; Neus, S.; Bakarinow, K.; Fey, M. Thermal Behavior of Externally Driven Spindle: Experimental Study and Modelling. Engineering 2015, 7, 73–92.

[13] Bossmanns B, Tu J F. A power flow model for high speed motorized spindles—heat generation characterization[J]. J. Manuf. Sci. Eng., 2001, 123(3): 494-505.

[14] Bossmanns B, Tu J F. A thermal model for high speed motorized spindles[J]. International Journal of Machine Tools and Manufacture, 1999, 39(9): 1345-1366.

[15] Dittus F W, Boelter L M K. Heat Transfer in Automobile Radiators of the Tubular Type[J]. University of California Publications on Engineering, 1930, 2: 443-461.

[16] Liu Y, Ya-Xin M, Qing-Yu M, et al. Improved thermal resistance network model of motorized spindle system considering temperature variation of cooling system[J]. Advances in Manufacturing, 2018, 6(4): 384-400.

[17] Yang Y, Xiao Y, Du Z, et al. Data-driven varying state-space model based on thermal network for transient temperature field prediction of motorized spindles[J]. Applied Thermal Engineering, 2023, 219: 119456.

[18] Zhang, Naijia; Zhou, Jingzhi; Huai, Xiulan; Zhou, Feng; Chen, Qihan; Jiang, Yawen; Experimental Study on Thermal Enhancement of a Pump-Assisted Loop Heat Pipe Based on Superhydrophilic Multiscale Composite. Journal of Thermal Science, 2025, 34(5): 1937-1952. http://dx.doi.org/10.1007/s11630-025-2130-5

[19] Amiri Delouei, Amin; Emamian, Amin; Ghorbani, Saeed; Khorrami, Aref; Jafarian, Karim; Sajjadi, Hasan; Atashafrooz, Meysam; Jing, Dengwei; Tarokh, Ali; A Review on Analytical Heat Transfer in Functionally Graded Materials, Part I: Fourier Heat Conduction. Journal of Thermal Science, 2025, 34(4): 1358-1386. http://dx.doi.org/10.1007/s11630-025-2112-7

[20] Cheng Y, Zhang X, Zhang G, et al. Thermal error analysis and modeling for high-speed motorized spindles based on LSTM-CNN[J]. The International Journal of Advanced Manufacturing Technology, 2022, 121: 3243-3257.

[21] Liu Z, Wei K, Chen C, et al. Thermal error recognition and prediction method for economical motorized spindles based on thermal characteristics knowledge graph[J]. Pattern Recognition Letters, 2025, 189: 229-238.

[22] Peng J, Yang K, Zhang Z, et al. Dynamic modeling for spindle thermal error in machine tools under time-varying rotational speeds and cooling states[J]. Case Studies in Thermal Engineering, 2026: 107733.